



## 33 **Abstract**

34

35 Changes in atmospheric composition, such as increasing greenhouse gases, cause an initial  
36 radiative imbalance to the climate system, quantified as the instantaneous radiative forcing. This  
37 fundamental metric has not been directly observed globally and previous estimates have come  
38 from models. In part, this is because current space-based instruments cannot distinguish the  
39 instantaneous radiative forcing from the climate's radiative response. We apply radiative kernels  
40 to satellite observations to disentangle these components and find all-sky instantaneous radiative  
41 forcing has increased  $0.53 \pm 0.11$  W/m<sup>2</sup> from 2003 through 2018, accounting for positive trends in  
42 the total planetary radiative imbalance. This increase has been due to a combination of rising  
43 concentrations of well-mixed greenhouse gases and recent reductions in aerosol emissions. These  
44 results highlight distinct fingerprints of anthropogenic activity in Earth's changing energy  
45 budget, which we find observations can detect within 4 years.

46

## 47 **Plain Language Summary**

48 Climate change is a response to energy imbalances in the climate system. For example, rising  
49 greenhouse gases directly cause an initial imbalance, the radiative forcing, in the planetary  
50 radiation budget, and surface temperatures increase in response as the climate attempts to restore  
51 balance. The radiative forcing and subsequent radiative feedbacks dictate the amount of  
52 warming. While there are well-established observational records of greenhouse gas  
53 concentrations and surface temperatures, there is not yet a global measure of the radiative  
54 forcing, in part because current satellite observations of Earth's radiation only measure the sum  
55 total of radiation changes that occur. We use the radiative kernel technique to isolate radiative

56 forcing from total radiative changes and find it has increased from 2003 through 2018,  
 57 accounting for nearly all of the long-term growth in the total top-of-atmosphere radiation  
 58 imbalance during this period. We confirm that rising greenhouse gas concentrations account for  
 59 most of the increases in the radiative forcing, along with reductions in reflective aerosols. This  
 60 serves as direct evidence that anthropogenic activity has affected Earth’s energy budget in the  
 61 recent past.

62  
 63 **1. Introduction**

64  
 65 The Instantaneous Radiative forcing (IRF) is the initial imbalance of the Earth’s top-of-  
 66 the-atmosphere (TOA) radiative energy budget directly caused by a change in atmospheric  
 67 composition, such as increasing greenhouse gases (GHGs), or perturbed surface properties, like  
 68 from land use change. All anthropogenic climate changes are a response to the IRF, including  
 69 surface temperature change and associated radiative feedbacks (Sherwood et al. 2015). Despite a  
 70 sound basis in physics and radiative transfer theory, the IRF is hard to directly diagnose from  
 71 observations. Multiple remote sensing and in-situ instruments observe net radiative fluxes, but  
 72 these measurements convolve the IRF with radiative responses to the changing atmospheric  
 73 state. Some studies have diagnosed a more broadly defined “greenhouse effect” by evaluating  
 74 observations of clear-sky longwave radiation at the surface (Philipona et al. 2004) and TOA  
 75 (Raghuraman et al. 2019), but this analysis does not separate the IRF from water vapor feedback  
 76 processes.

77 Harries et al. (2001) compared outgoing longwave radiation at the TOA from two  
 78 satellite instruments launched decades apart, attributing emission differences at relevant spectral  
 79 bands to rising greenhouse gas (GHG) concentrations. However, instrumental uncertainty  
 80 between the two platforms complicates interpretation (Jiang et al. 2011). Feldman et al. (2015,

81 2018) used ground observations from the US Department of Energy Atmospheric Radiation  
 82 Measurement (ARM) program to provide the most observationally-oriented assessment to date  
 83 of GHG surface radiative forcing, which is proportional to the TOA IRF. However, their  
 84 analysis was limited to longwave (LW) forcing from CO<sub>2</sub> and CH<sub>4</sub> and was only conducted for  
 85 two locations. The total IRF has not been directly diagnosed globally from observations.

86 Well understood radiative transfer theory tightly constraints the GHG component of the IRF.  
 87 Line-by-line radiative transfer models diagnose it within 1% agreement (Collins et al. 2006;  
 88 Mlynczak et al. 2016; Pincus et al. 2020). However, these highly accurate calculations are  
 89 computationally expensive, so analysis is often limited to a few idealized atmospheric profiles.  
 90 Quantifying the IRF globally and over time relies on more efficient but less accurate  
 91 parameterized radiative transfer models (Soden et al. 2018), which introduces model bias when  
 92 applied to observations. Diagnosing the IRF from aerosols with these models suffers from the  
 93 same pitfalls, plus additional uncertainty associated with aerosol optical properties that are not  
 94 well-observed (Randles et al. 2013; Stier et al. 2013). While there have been recent efforts to  
 95 constrain aerosol IRF with observations (Bellouin et al. 2020; Watson-Parris et al. 2020), results  
 96 are usually not temporally resolved.

97 Here we circumvent these limitations by applying radiative kernels (Soden et al. 2008) to  
 98 isolate the IRF from radiative feedbacks and rapid adjustments over time. We demonstrate that  
 99 the IRF has increased with rising GHG concentrations, accounting for recent, positive trends in  
 100 the total TOA radiative imbalance. More specifically, we consider this IRF to be largely a  
 101 consequence of concentration changes after anthropogenic emissions are moderated by natural  
 102 carbon cycle responses (Friedlingstein et al. 2019).

103

104 **2. Methods**

105

106

107

108

109

110

111

112

113

114

115

116

117

118

119

120

121

122

123

124

125

126

127

Variations in the total, all-sky radiative energy balance at the TOA,  $dR$ , constrain global surface temperature change and consists of the all-sky instantaneous radiative forcing (IRF) and radiative responses to the IRF:

$$dR = IRF + dR_{\lambda} \quad (1),$$

where  $dR_{\lambda}$  is net radiative changes caused by surface temperature-mediated radiative feedbacks and rapid adjustments from, to first order, temperature ( $T$ ), water vapor ( $q$ ), surface albedo ( $\alpha$ ) and cloud ( $C$ ) changes (Vial et al. 2013; Sherwood et al. 2015):

$$dR_{\lambda} = dR_T + dR_q + dR_{\alpha} + dR_C \quad (2).$$

For simplicity, we will not decompose these terms further into feedbacks and rapid adjustments since it has no bearing on diagnosing the IRF. We simply refer to these radiative anomalies as radiative responses. We note that  $dR_{\lambda}$  includes both anthropogenic responses and natural variability (e.g. Trenberth et al. 2015).

The Clouds and Earth’s Radiant Energy System (CERES) has provided global TOA energy balance observations since 2000. Here, we diagnose  $dR$  using radiative flux anomalies from the CERES Energy Balance and Filled (EBAF) Ed. 4.1 product (Loeb et al. 2018a; Loeb et al. 2019). While no observational product measures the radiative response terms in isolation, they can be diagnosed using radiative kernels combined with observations of the relevant state

128 variable,  $x$  (B. Zhang et al. 2019; Bony et al. 2020). An individual, non-cloud radiative response,  
 129  $dR_x$ , in linear form is:

130

$$131 \quad dR_x = \frac{\partial R}{\partial x} dx = K_x dx, \quad x = T, q, \alpha \quad (3),$$

132

133 where  $K_x$  is a radiative kernel representing direct radiative changes from small, standard  
 134 perturbations in state variable  $x$  and  $dx$  is the actual temperature ( $T$ ), water vapor ( $q$ ) or surface  
 135 albedo ( $\alpha$ ) climate response. Under clear-sky (CS) conditions:

$$136 \quad dR^{CS} = IRF^{CS} + dR_\lambda^{CS} \quad (4),$$

137

138 where:

$$139 \quad dR_\lambda^{CS} = dR_T^{CS} + dR_q^{CS} + dR_\alpha^{CS} \quad (5).$$

140

141 To diagnose  $dR_x$  or  $dR_x^{CS}$  we use observational-based radiative kernels developed from  
 142 the CloudSat Fluxes and Heating Rates product 2B-FLXHR-LIDAR (Kramer et al. 2019).  
 143 Unlike GCM-derived radiative kernels, these kernels are free from model bias in the base state,  
 144 and thus ideal for diagnosing observed radiation changes. Calculating  $K_x$  requires using a  
 145 radiative transfer model to convert base state perturbations to radiative sensitivities. Therefore,  
 146 using radiative kernels introduces some radiative-transfer model dependency. We apply the  
 147 radiative kernels to deseasonalized anomalies of temperature and specific humidity profiles from  
 148 version 6 Level 3 AIRS retrievals (Aumann et al. 2003) to estimate  $dR_T$  and  $dR_q$  and to surface  
 149 albedo anomalies from CERES EBAF surface fluxes (Kato et al. 2018) to estimate  $dR_\alpha$ . Due to  
 150 computational expense, radiative kernels, including those used here, are often derived from one

151 year of data. However radiative kernel inter-annual variability is small (Pendergrass et al. 2018;  
 152 Thorsen et al. 2018), therefore applying radiative kernels to the entire observational record is  
 153 justified.

154 In the traditional radiative kernel technique used here, the cloud radiative response ( $dR_C$ )  
 155 is calculated as the change in cloud radiative effects (CRE) corrected for cloud masking (Soden  
 156 et al, 2008; Kramer et al. 2019):

157

$$158 \quad dR_C = dCRE - (dR_T - dR_T^{CS}) - (dR_q - dR_q^{CS}) - (dR_\alpha - dR_\alpha^{CS}) - (IRF - IRF^{CS}) \quad (6),$$

159

160 where CRE is the difference between all-sky and clear-sky radiative fluxes. The cloud masking  
 161 correction is necessary because CRE includes differences between all-sky and clear-sky non-  
 162 cloud radiative changes, which are not actual cloud radiative responses (Soden et al. 2004). Here  
 163  $dCRE$  is estimated using the TOA CERES EBAF radiative fluxes. The  $dR_x$  terms are diagnosed  
 164 using all-sky and clear-sky radiative kernels as described above.

165 The ultimate goal of this study is to derive the IRF from these radiative kernel  
 166 calculations. Under clear-sky conditions, we simply diagnose  $IRF^{CS}$  by rearranging Equation 3,  
 167 whereby:

168

$$168 \quad IRF^{CS} = dR^{CS} - dR_\lambda^{CS} = dR^{CS} - (dR_T^{CS} + dR_q^{CS} + dR_\alpha^{CS}) \quad (7),$$

169

170 For all-sky conditions, an analogous calculation would require  $dR_C$  to be removed from  $dR$ , but  
 171 since estimating  $dR_C$  as in equation 6 requires the IRF to be known, this differencing technique is  
 172 not possible. Following common practice (Soden et al. 2008; Vial et al. 2013), we estimate the  
 173 all-sky IRF as:

174 
$$IRF = \frac{IRF^{CS}}{Cl} \quad (8),$$

175  
 176 where  $Cl$  is a constant that accounts for cloud masking of the IRF. For the longwave (LW)  $Cl$ ,  
 177 we use a constant of 1.24, derived by dividing clear-sky and all-sky double-call radiative transfer  
 178 calculations of  $CO_2$  IRF from models (Smith et al. 2018). The cloud mask for the shortwave  
 179 (SW) is derived from direct output of aerosol IRF from Modern-Era Retrospective Analysis for  
 180 Research and Applications, Version 2 (MERRA-2) reanalysis (Gelaro et al. 2017). The global-  
 181 mean value is 2.43, in line with a range of observational-based cloud masking estimates by  
 182 Bellouin et al. (2020). Only the MERRA-2 SW  $Cl$  is available over time, but it has an  
 183 insignificant long-term trend. Consequently, SW IRF has nearly identical trends when computed  
 184 with a time resolved versus constant SW  $Cl$ .

185         This conversion to all-sky conditions accounts for the presence of clouds but not cloud  
 186 changes. Therefore, the IRF in this study does not include aerosol-cloud interactions, such as  
 187 cloud albedo effects (Boucher et al. 2013). Instead, these terms are included in  $dR_C$ . Therefore,  
 188 the aerosol component to the kernel-derived estimates of IRF is akin to aerosol direct radiative  
 189 effects found throughout the literature (e.g. Thorsen et al. 2020).

190         The AIRS L3 data has the shortest record among satellite observations used in this study,  
 191 with 2003 being the first complete year of data. Thus, we compute all deseasonalized anomalies  
 192 from 2003 through 2018 relative to the mean of that time span. While we refer to the resulting  
 193 calculation as the IRF for brevity, we actually show anomalies of the IRF. For comparison, we  
 194 also estimate the IRF by applying the CloudSat radiative kernels to MERRA-2 reanalysis over  
 195 the same period. This reanalysis product assimilates a variety of satellite observations, including  
 196 observations of aerosol properties.



197 In climate models, idealized simulations and flux diagnostics from double-call radiative  
198 transfer calculations can be used to evaluate the accuracy of radiative kernel estimates of  $dR_{\lambda}$  and  
199 IRF (e.g. Vial et al. 2013; Smith et al. 2018). Such a comparison is not possible in the observed  
200 record or the MERRA-2 reanalysis, however. Since the IRF is derived from differencing the  
201 other radiative terms, there will always be near-perfect energy closure, albeit with some error due  
202 to cloud masking assumptions, which is typically small (Chung and Soden 2015). Alternatively,  
203 we will compare these kernel-derived estimates to various independent measures of the IRF.

204 To verify the aerosol component of the IRF, we compare radiative kernel-derived SW  
205 IRF to direct output of the aerosol direct radiative effect from MERRA-2. We also compare SW  
206 IRF to trends in aerosol optical depth (AOD) from MERRA-2 and observations from the  
207 Moderate Resolution Imaging Spectroradiometer (MODIS) merged Dark Target and Deep Blue  
208 product (Sayer et al. 2014).

209 We compare radiative-kernel derived estimates of the LW IRF to offline radiative  
210 transfer calculations of GHG IRF. We apply empirical formulas to observed global-mean  
211 concentrations of 5 major greenhouse gases ( $\text{CO}_2$ ,  $\text{CH}_4$ ,  $\text{N}_2\text{O}$ , CFC-11 and CFC-12), provided by  
212 NOAA Global Monitoring Division (Hoffman et al. 2006; Montzka et al. 2011). Etminan et al.  
213 (2016) derive the empirical formulas from polynomial fits to line-by-line radiative forcing  
214 calculations. While these formulas were originally developed for net stratospherically adjusted  
215 radiative forcing, we use corrections from additional line-by-line calculations (Hodnebrog et al.  
216 2013; Etminan et al. 2016) to calculate TOA IRF, decomposed into a LW and SW component.

217 We also estimate GHG IRF using the SOCRATES offline radiative transfer model  
218 (Edwards et al. 1996; Manners et al. 2015) with NOAA GHG concentrations and atmospheric  
219 profiles from the MERRA-2 reanalysis. Like the other IRF estimates, these calculations are

220 presented in anomaly space with the seasonal cycle removed. The IRF from CFCs has decreased  
221 recently, but this has been compensated for by a near equal increase from other halocarbons not  
222 considered in empirical fit and SOCRATES calculations (Myhre et al. 2013a). To account for  
223 this, we repeat these calculations with no CFC trend. This only modifies total GHG IRF trends  
224 by <5%, however, so hereafter we focus on results without this assumption. The SOCRATES  
225 IRF calculations are conducted under pristine, clear-sky conditions and converted to all-sky via  
226 Equation 8, like the radiative kernel calculations.

227 The various inputs and assumptions detailed above can contribute uncertainty to the  
228 estimated radiative changes. In a Supplemental Appendix we provide a comprehensive  
229 uncertainty assessment in the IRF trends due to these contributors, including from observed  $dR$ ,  
230 radiative kernels, and the cloud masking constant,  $Cl$ . We find these uncertainties are smaller  
231 than the trend regression uncertainty associated with timeseries variability. Therefore, all trends  
232 presented hereafter are provided with 95% confidence intervals (or roughly 2 standard errors  
233 around the mean) associated with the least-squares linear regression. This is common practice  
234 when diagnosing CERES trends (e.g. Loeb et al. 2018a,b).

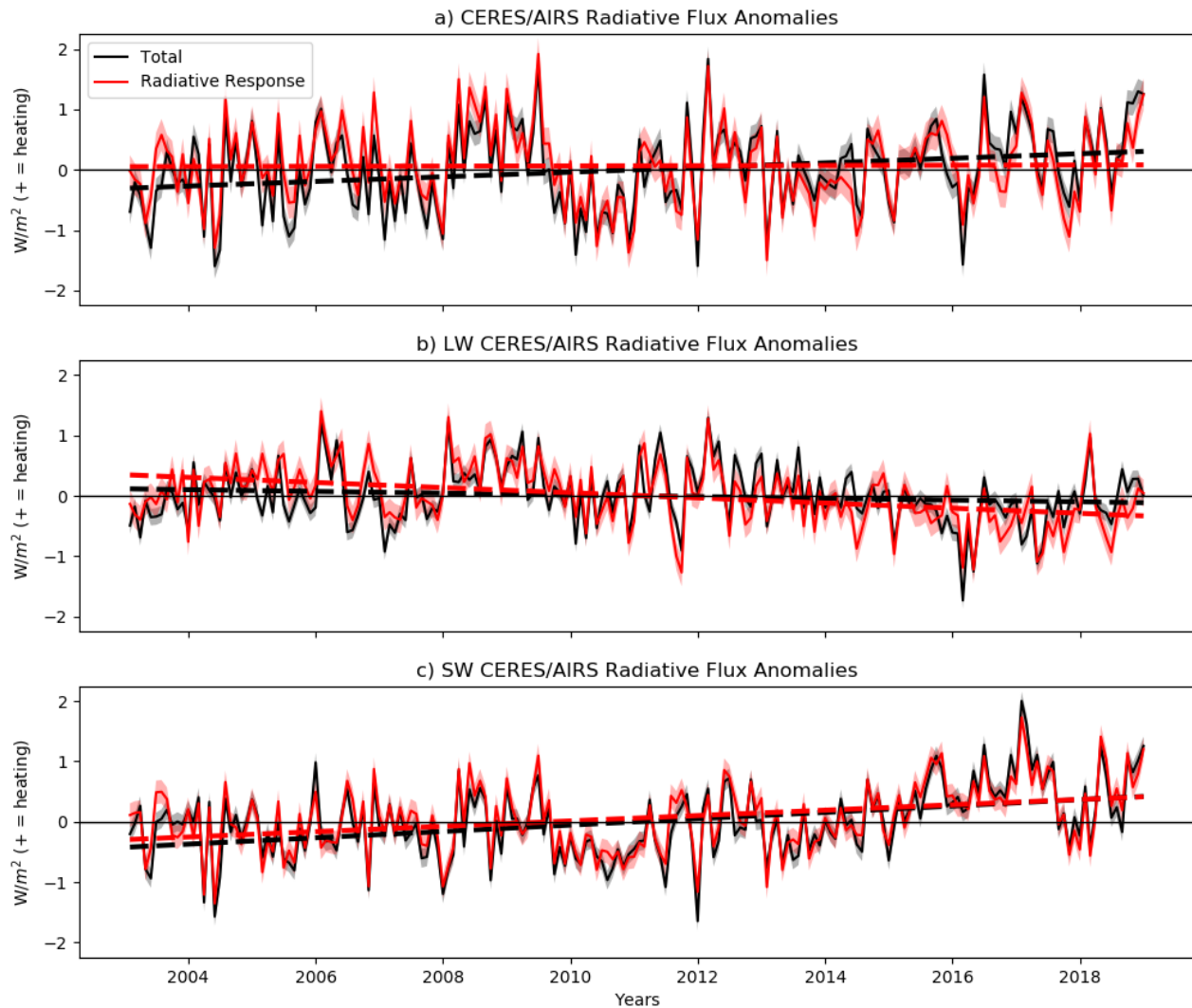
235 The anomalies of  $dR$ ,  $dR_\lambda$  and the IRF are subject to the same sources of uncertainty as long-  
236 term trends. Therefore, Figure 1 and 2 below include uncertainty bounds diagnosed as  $2\sigma$  across  
237 multiple estimates of the radiative terms using different radiative flux data products from CERES  
238 and alternative radiative kernel sets and model estimates of  $Cl$  (see Supplemental Appendix).

### 239 240 **3. Results**

241  
242  
243 Figure 1a shows a timeseries of global-mean total radiative flux anomalies ( $dR$ ) from CERES  
244 satellite observations and its component from radiative responses ( $dR_\lambda$ ), estimated by applying

245 the CloudSat-based radiative kernels to CERES and AIRS observations (hereafter  
 246 CERES/AIRS). Positive anomalies indicate a net increase in downwelling radiation at the TOA  
 247 (planetary warming). The sum of the radiative responses,  $dR_\lambda$ , accounts for nearly all of the total  
 248 short-term  $dR$  variability, as evident by their strong correlation ( $r=0.88$ ) and small root-mean-  
 249 squared difference of  $0.024 \pm 0.003 \text{ W/m}^2$ ;  $\sim 3.5\%$  of the standard deviation of  $dR$ . On inter-annual  
 250 timescales, ENSO strongly influences this variability (Trenberth et al. 2014), which lags by  $\sim 5$   
 251 months (Supplemental Fig. S1; Loeb et al. 2018b). Long-term  $dR$  exhibits a positive, linear trend  
 252 ( $0.038 \pm 0.02 \text{ W/m}^2/\text{year}$ ) significant with 95% confidence, while  $dR_\lambda$  exhibits an insignificant  
 253 trend ( $0.002 \pm 0.02 \text{ W/m}^2/\text{year}$ ) an order of magnitude smaller. This arises from cancelation  
 254 between LW and SW  $dR_\lambda$ . The LW  $dR_\lambda$  has a negative linear trend ( $-0.042 \pm 0.02 \text{ W/m}^2/\text{year}$ )  
 255 (Fig. 1b), mainly from global warming-driven  $dR_T$  decreases ( $-0.041 \pm 0.007 \text{ W/m}^2/\text{year}$ )  
 256 (Supplemental Fig. S2). The SW  $dR_\lambda$  trend ( $0.044 \pm 0.02 \text{ W/m}^2/\text{year}$ ) is nearly equal and opposite  
 257 of the LW, driven by increases in SW  $dR_\alpha$  ( $0.023 \pm 0.09 \text{ W/m}^2/\text{year}$ ) and SW  $dR_C$  ( $0.020 \pm 0.13$   
 258  $\text{W/m}^2/\text{year}$ ), a predominantly low cloud response (Loeb et al. 2018b). The latter alone accounts  
 259 for most of the SW interannual variability.

260



261

262

263 **Figure 1.** Global-mean a) net, b) longwave (LW) and c) shortwave (SW) total radiative flux  
 264 anomalies from 2003 through 2018 as measured by CERES (black) and the contribution to that  
 265 total from the sum of radiative responses (red). Respective trendlines are displayed as dashed  
 266 lines. Uncertainty of  $\pm 2\sigma$  is shown for each timeseries, computed as described in the Methods.  
 267 Linear trends and 95% confidence intervals are provided in text.

268

269

270

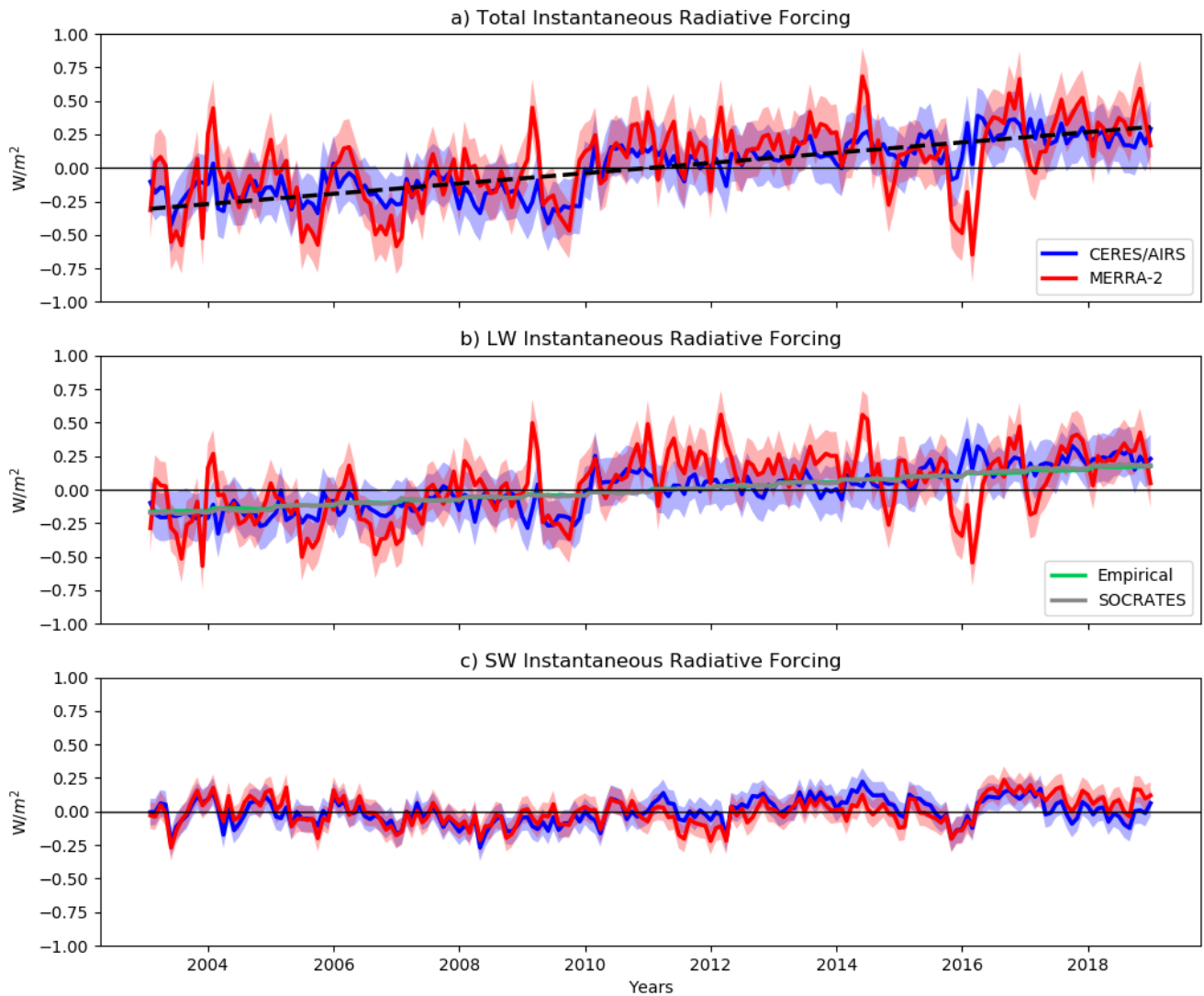
271

272

MERRA-2 also exhibits a significant, positive trend in  $dR$  but not  $dR_\lambda$  due to compensating  
 LW and SW components (Supplemental Fig. S3). However, there is a positive trend in LW  $dR_\lambda$   
 and a negative trend in SW  $dR_\lambda$ , opposite from the CERES/AIRS response. This occurs due to a  
 considerably different LW and SW  $dR_C$  (Supplemental Fig. S4) compared to satellite  
 observations.

273            Since neither  $dR_\lambda$  or its uncertainties account for the positive  $dR$  trend, it must be  
 274 explained by the IRF. Figure 2 shows the timeseries of the total, LW and SW IRF under all-sky  
 275 conditions, estimated from the radiative kernel technique. The total CERES/AIRS IRF exhibits a  
 276 significant, positive trend ( $0.033\pm 0.007$  W/m<sup>2</sup>/year), mostly from increasing LW IRF  
 277 ( $0.027\pm 0.006$  W/m<sup>2</sup>/year). The SW IRF exhibits a smaller, yet still significant increase  
 278 ( $0.006\pm 0.003$  W/m<sup>2</sup>/year). The LW IRF trend is opposite in sign from LW  $dR$ , since decreasing  
 279 LW  $dR_\lambda$  compensates. In the SW, IRF and  $dR$  are both increasing, but SW  $dR_\lambda$  is the dominant  
 280 contributor while the IRF trend is much smaller.

281            Rising GHG concentrations explain the positive LW IRF trend. Accordingly, it increases  
 282 at a similar rate to the GHG IRF estimates from the empirical fit ( $0.021\pm 0.0002$  W/m<sup>2</sup>/year or  
 283  $0.022\pm 0.0002$  W/m<sup>2</sup>/year if ignoring CFCs [see Methods]) and the SOCRATES radiative  
 284 transfer model ( $0.023\pm 0.0003$  W/m<sup>2</sup>/year) (Fig. 2b), despite these calculations neglecting some  
 285 GHG forcers found in nature, such as ozone. MERRA-2 exhibits a similar LW IRF trend to  
 286 CERES/AIRS ( $0.029\pm 0.003$  W/m<sup>2</sup>/year) while direct output of the LW aerosol IRF from  
 287 MERRA-2 exhibits no trend. This further indicates GHG increases account for roughly all LW  
 288 IRF increases.



289

290

291 **Figure 2.** Global-mean a) total, b) longwave (LW) and c) shortwave (SW) instantaneous  
 292 radiative forcing (IRF) estimated from the radiative kernel technique for CERES/AIRS (red) and  
 293 MERRA-2 (blue). Additional calculations of greenhouse gas-only IRF are also shown using  
 294 empirical formulas (green) and the SOCRATES radiative transfer model (gray). For reference,  
 295 the trendline for total radiative flux anomalies (Fig 1a) is displayed with the total IRF as a black  
 296 dashed line. Uncertainty of  $\pm 2\sigma$  is shown with shading for each timeseries, computed as  
 297 described in the Methods. Linear trends and 95% confidence intervals are provided in text and  
 298 in Table 1.

299

Increasing GHG concentrations also contribute ( $0.002 \pm 0.00$  W/m<sup>2</sup>/year) to the total

300

positive SW IRF trends, according to estimates from the empirical fits. The SW GHG trend is

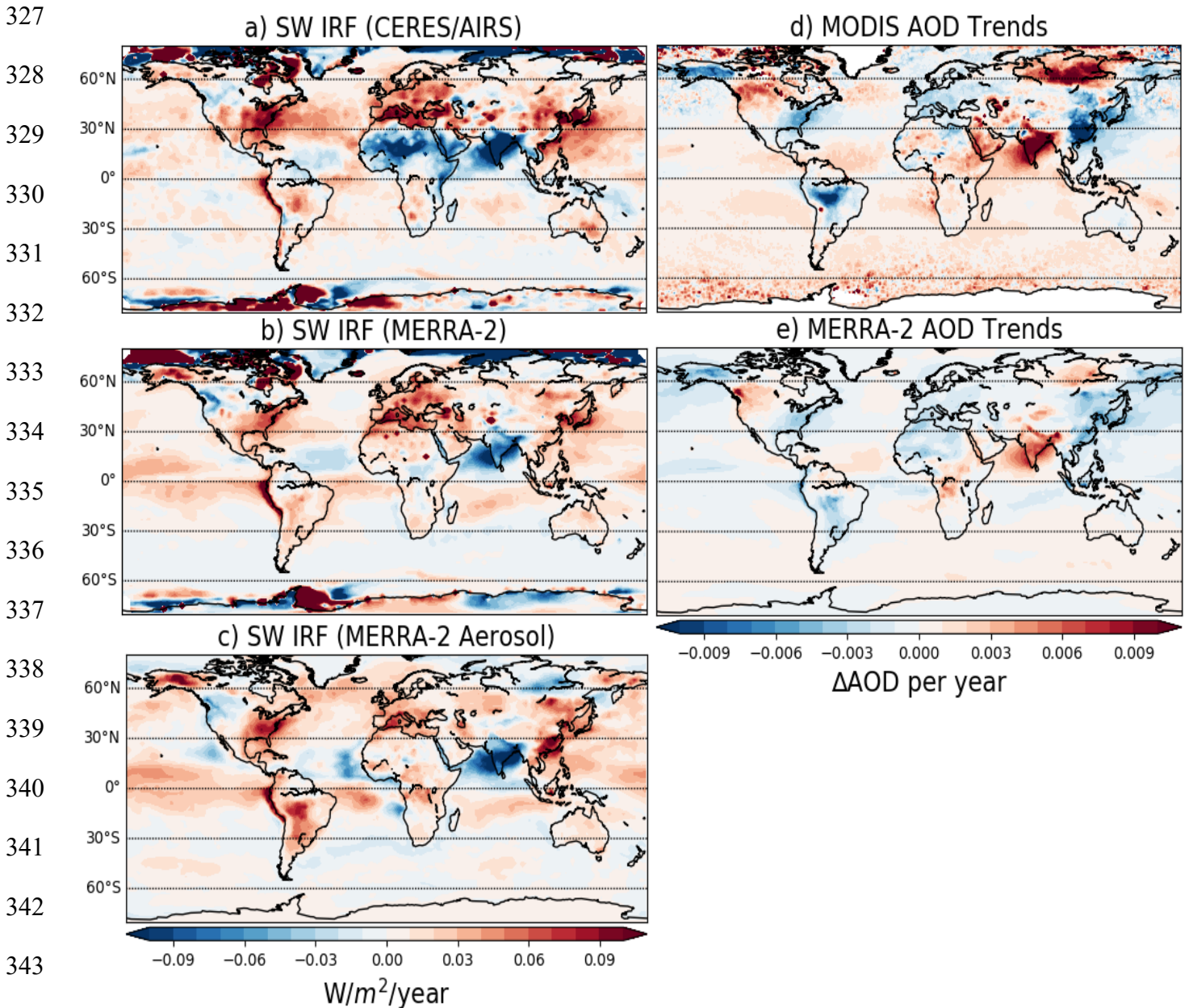
301 negligible in the SOCRATES calculations, but the model version used here does not account for  
 302 the SW absorption of CH<sub>4</sub>.

303 The total SW IRF increase is nearly identical in CERES/AIRS and MERRA-2, and to  
 304 aerosol-only SW IRF trends from MERRA-2 direct output (Supplemental Fig. S5). They also  
 305 exhibit similar short-term variability. This suggests aerosols explain most of the SW IRF. The  
 306 long-term radiative heating is consistent with declining anthropogenic aerosol emissions during  
 307 this period (Q. Zhang et al. 2019). Towards the end of the timeseries, CERES/AIRS SW IRF has  
 308 more positive anomalies. Locally, the largest differences with MERRA-2 after 2015 are in major  
 309 absorbing aerosol source regions (Supplemental Fig. S6), suggesting a contribution from  
 310 different absorbing aerosol properties.

311 Figure 3 shows local linear trends in kernel-derived, total SW IRF from CERES/AIRS  
 312 and MERRA-2 and direct MERRA-2 output of aerosol-only SW IRF (Figure 3c). The spatial  
 313 pattern of the SW IRF trend is generally consistent across all three estimates. A notable  
 314 hemispheric asymmetry is present, with large changes concentrated in the populous Northern  
 315 Hemisphere. This includes large positive trends over the Eastern United States, Western Europe  
 316 and Eastern China, where anthropogenic emissions of reflective aerosols have declined because  
 317 of government actions to combat poor air quality (Kühn et al. 2014; Ridley et al. 2018; Q. Zhang  
 318 et al. 2019). In contrast, the SW IRF trends are negative over India, where emissions continue to  
 319 rise (Dey et al. 2012).

320 There are some magnitude differences in these major source regions, however. For  
 321 instance, trends are larger in the Eastern US and India in CERES/AIRS than in MERRA-2. This  
 322 coincides with differences in the MODIS and MERRA-2 AOD trends (Figure 3d,e), which are  
 323 also larger in CERES/AIRS. Over Saharan Africa, the sign of the SW IRF trend differs,

324 consistent with opposing trends in MODIS and MERRA-2 AOD. Dust radiative forcing during  
 325 this period is likely a key factor (Supplemental Fig. S7; Shao et al. 2013) and is highly uncertain  
 326 (Miller et al. 2014; Kok et al. 2017).



345 **Figure 3.** Local linear trends from 2003 through 2018 in all-sky shortwave instantaneous radiative forcing  
 346 (SW IRF) diagnosed in a) CERES/AIRS observations and b) MERRA-2 reanalysis using the radiative kernel  
 differencing technique and c) from direct output of MERRA-2 aerosol IRF. Also, local linear trends over the  
 same time period are shown for aerosol optical depth (AOD) from d) MODIS and e) MERRA-2.



347  
 348  
 349           The strong agreement in MERRA-2 trends from kernel differencing versus direct SW  
 350 aerosol IRF output (Fig 3b,c) highlights the dominant role of aerosols in the total SW IRF trends.  
 351 It also confirms the accuracy of the radiative kernel technique. The kernel differencing method  
 352 results in artifacts in the polar regions, however, where large local trends are a consequence of  
 353 underestimating the SW  $dR_{\alpha}$  removed from  $dR$  (Supplemental Fig. S8) and not from actual  
 354 forcing. One possible explanation is surface albedo radiative kernels fail to capture important  
 355 ice-albedo feedback non-linearities (Block and Mauritsen 2013). Nevertheless, the polar region  
 356 errors have negligible effect on global-mean SW IRF trends.

357           Some inter- and intra-annual variability (hereafter short-term variability) in SW IRF is  
 358 expected, given natural variations in aerosol concentrations. Consequently, the detrended  
 359 aerosol-only ( $\sigma=0.088$  W/m<sup>2</sup>) and kernel-derived ( $\sigma=0.097$  W/m<sup>2</sup>) SW IRF in MERRA-2  
 360 exhibit similar variability and are highly correlated ( $r=0.78$ ). The source of the notable short-  
 361 term variability in LW IRF (Fig. 2b) is less apparent, however, since greenhouse gas  
 362 concentrations increase relatively steadily on these timescales, as evident in the empirical fit  
 363 estimate of GHG IRF, which increases almost perfectly linearly.

364           While radiative kernel error may play some role, the LW IRF from CERES/AIRS  
 365 exhibits considerably more short-term variability ( $\sigma=0.24$ ) than MERRA-2 ( $\sigma=0.16$ ), despite  
 366 using the same CloudSat-derived radiative kernels in both estimates. This highlights short-term  
 367 inconsistencies between the radiative fluxes observed by CERES ( $dR^{cs}$ ) and the AIRS retrievals  
 368 used to diagnose LW  $dR_{\lambda}^{cs}$ . For instance, the difference between CERES/AIRS and MERRA-2  
 369  $dR_{\lambda}^{cs}$  exhibits considerably more short-term variability than the difference between  $dR^{cs}$ . This is  
 370 mostly due to different variability in  $dR_{\tau}^{cs}$  (Supplemental Fig. S9), and more specifically due to

371 different temperature anomalies at the surface and in the boundary layer between AIRS and  
 372 MERRA-2 (Supplemental Fig. S10). Since AIRS temperature anomalies are more variable, so is  
 373 the  $dR_T^{cs}$  estimate. And since this variability is not also observed radiatively by CERES, it is not  
 374 evident in  $dR^{cs}$ . This ultimately translates to a more variable LW IRF when using the kernel  
 375 differencing technique. This also explains why LW IRF spatial patterns are noisier for  
 376 CERES/AIRS than for MERRA-2 (Supplemental Fig. S11). Cloud contamination likely  
 377 contributes to the AIRS temperature variability, as found previously (Hearty et al. 2014). This is  
 378 evident at the surface, for example, where the largest differences between AIRS and MERRA-2  
 379 temperature anomalies tend to occur where clouds are common (Supplemental Fig. S9),  
 380 especially over land. While global-mean surface temperature anomalies from AIRS closely agree  
 381 with other, independent datasets (Susskind et al. 2019), it is possible the temperature biases that  
 382 do exist are magnified in the context of radiative changes.

383         The LW IRF variability may also stem from its sensitivity to the atmospheric base state  
 384 (Pincus et al. 2015). However, this contribution appears to be small. In the LW GHG IRF  
 385 estimated from the SOCRATES radiative transfer model, we use daily MERRA-2 temperature,  
 386 surface albedo and humidity data, thus capturing the GHG IRF sensitivity to the unperturbed,  
 387 non-cloud base state. Still, the short-term variability from this offline calculation is nearly as  
 388 small as estimates with the empirical fit, which does not account for base state variability. The  
 389 LW IRF short-term variability in this comparison (and in the radiative kernel-derived estimates)  
 390 is not due to variations in the cloud base state since LW cloud masking is always treated as a  
 391 constant. While clouds may play a greater role in reality, the SW IRF estimated from radiative  
 392 kernels with constant cloud masking has similar short-term variability to the aerosol-only SW  
 393 IRF in MERRA-2, which accounts for cloud masking temporal variations. This suggests cloud

394 variability may not be important in the global-mean. Lastly, some LW IRF variability in  
 395 MERRA-2 (and in CERES/AIRS) may be due to spatial variability in the GHG concentrations  
 396 (Myhre et al. 2013a), which is not present in the empirical fit or the SOCRATES estimates.

397

	LW	SW	Net
CERES/AIRS	0.027±0.006	0.006±0.003	0.033±0.007
MERRA-2	0.029±0.003	0.006±0.003	0.035±0.004
Aerosol-Only MERRA-2	-4.2E-4±1.5E-4	0.006±0.003	0.006±0.003

398 **Table 1.** Global-mean linear trends ( $W/m^2/year$ ) and 95% confidence bounds in  
 399 instantaneous radiative forcing estimated using the radiative kernel differencing  
 400 technique (first two rows) and MERRA-2 flux diagnostics (third row).

401

402

403

404 **4. Conclusions**

405

406 We have diagnosed the global instantaneous radiative forcing (IRF) directly from  
 407 observations using radiative kernels. Table 1 summarizes linear trends. We find that from 2003  
 408 through 2018, the observed IRF has increased  $0.53 \pm 0.11 W/m^2$ , almost entirely accounting for  
 409 the positive trend in CERES Top-of-Atmosphere (TOA) radiative flux anomalies ( $dR$ ). The  
 410 intrinsic LW and SW climate radiative responses largely cancel out. This IRF increase mostly  
 411 occurs in the LW ( $0.43 \pm 0.1 W/m^2$ ), driven by rising greenhouse gas concentrations. This serves  
 412 as direct observational evidence that anthropogenic activity is impacting the Earth's energy  
 413 balance. The SW IRF has also increased ( $0.1 \pm 0.05 W/m^2$ ). In part, this is a reflection of  
 414 government-mandated aerosol emission reductions throughout major source regions, which may  
 415 have a greater direct impact than inferred by the SW IRF, which does not include aerosol cloud-  
 416 albedo effects in this analysis.

417 Diagnosing the observed IRF is important for our fundamental understanding of Earth's  
 418 response to climate change and a valuable piece of information for policy decisions.  
 419 Conceivably, observed IRF could be used as a top-down approach for monitoring the climate  
 420 response to mitigation efforts. By applying published metrics of instrumental uncertainty in  
 421 AIRS (Tobin et al. 2006; Hearty et al. 2014) and CERES (Loeb et al. 2018a), along with the  
 422 kernel-derived IRF variance and trend, we apply formulas by Leroy et al. (2008) to determine the  
 423 minimum length of the observational record necessary to detect a climate change signal. These  
 424 formulas account for trend uncertainty due to natural variability and instrumental uncertainty.  
 425 Using this approach, we find total IRF trends are detectable, given these sources of uncertainty,  
 426 within 3.8 years using the satellite data presented in this study. Therefore, the methods  
 427 introduced here could be useful for near-real time monitoring, especially since the time to  
 428 detection shortens with the lengthening of the observational record.

429

430 **Acknowledgements:** We thank the Editor, reviewers and Graeme Stephens for valuable  
 431 feedback on this work. RJK is supported by an appointment to the NASA Postdoctoral Program  
 432 administered by Universities Space Research Association. HH and BJS are supported by NASA  
 433 award 80NSSC18K1032. LO gratefully acknowledges support from NASA's  
 434 CloudSat/CALIPSO Science Team and MEaSUREs programs. GM, PMF and CJS were  
 435 supported by European Union's Horizon 2020 Research and Innovation Programme under grant  
 436 agreement no. 820829 (CONSTRAIN). PMF and CJS were also supported by UKRI NERC  
 437 grant NE/N006038/1 (SMURPHS). C.J.S. was supported by a NERC/IASA Collaborative  
 438 Research Fellowship (NE/T009381/1).

439

440 **Competing Interests:** Authors have no competing interests.

441

442 **Data and Materials Availability:** The CERES radiative flux observations are available at  
 443 <https://ceres.larc.nasa.gov/data/>. The AIRS temperature and water vapor observations and the  
 444 MERRA-2 reanalysis data are available at <https://disc.gsfc.nasa.gov/>. The CloudSat/CALIPSO  
 445 radiative kernels used in this study and related code for applying them are available at  
 446 <https://climate.rsmas.miami.edu/data/radiative-kernels/>.

447

448 **References**

449

450 Aumann, H.H., Chahine, M.T., Gautier, C., M. Goldberg, D., Kalnay, E., McMillin, L.M., et al.  
 451 (2003). AIRS/AMSU/HSB on the Aqua mission: design, science objectives, data products, and  
 452 processing systems. *IEEE Transactions on Geoscience and Remote Sensing*, 41(2), 253–264.  
 453 <https://doi.org/10.1109/TGRS.2002.808356>

454

455 Bellouin, N., Quaas, J., Gryspeerdt, E., Kinne, S., Stier, P., Watson-Parris, D., et al. (2020).  
 456 Bounding Global Aerosol Radiative Forcing of Climate Change. *Reviews of Geophysics*, 58(1),  
 457 e2019RG000660. <https://doi.org/10.1029/2019RG000660>

458

459 Block, K., & Mauritsen, T. (2013). Forcing and feedback in the MPI-ESM-LR coupled model  
 460 under abruptly quadrupled CO<sub>2</sub>. *Journal of Advances in Modeling Earth Systems*, 5(4), 676–691.  
 461 <https://doi.org/10.1002/jame.20041>

462

463 Bony, S., Semie, A., Kramer, R. J., Soden, B., Tompkins, A. M., & Emanuel, K. A. (2020).  
 464 Observed Modulation of the Tropical Radiation Budget by Deep Convective Organization and  
 465 Lower-Tropospheric Stability. *AGU Advances*, 1(3). <https://doi.org/10.1029/2019AV000155>

466

467 Boucher, O., Randall, D., Artaxo, P., Bretherton, C., Feingold, G., Forster, P., et al., (2013)  
 468 Clouds and aerosols. In *Climate Change 2013: The Physical Science Basis. Contribution of*  
 469 *Working Group I to the Fifth Assessment Report of the Intergovernmental Panel on Climate*  
 470 *Change*. T.F. Stocker, D. Qin, G.-K. Plattner, M. Tignor, S.K. Allen, J. Doschung, A. Nauels, Y.  
 471 Xia, V. Bex, and P.M. Midgley, Eds. Cambridge University Press, pp. 571-657,  
 472 doi:10.1017/CBO9781107415324.016.

473

474 Chung, E.-S., & Soden, B. J. (2015). An Assessment of Direct Radiative Forcing, Radiative  
 475 Adjustments, and Radiative Feedbacks in Coupled Ocean–Atmosphere Models\*. *Journal of*  
 476 *Climate*, 28(10), 4152–4170. <https://doi.org/10.1175/JCLI-D-14-00436.1>

477

- 478 Collins, W. D., Ramaswamy, V., Schwarzkopf, M. D., Sun, Y., Portmann, R. W., Fu, Q., et al.  
 479 (2006). Radiative forcing by well-mixed greenhouse gases: Estimates from climate models in the  
 480 Intergovernmental Panel on Climate Change (IPCC) Fourth Assessment Report (AR4). *Journal*  
 481 *of Geophysical Research*, *111*(D14), D14317. <https://doi.org/10.1029/2005JD006713>  
 482
- 483 Dey, S., Di Girolamo, L., van Donkelaar, A., Tripathi, S. N., Gupta, T., & Mohan, M. (2012).  
 484 Variability of outdoor fine particulate (PM<sub>2.5</sub>) concentration in the Indian Subcontinent: A  
 485 remote sensing approach. *Remote Sensing of Environment*, *127*, 153–161.  
 486 <https://doi.org/10.1016/j.rse.2012.08.021>  
 487
- 488 Edwards, J. M., & Slingo, A. (1996). Studies with a flexible new radiation code. I: Choosing a  
 489 configuration for a large-scale model. *Quarterly Journal of the Royal Meteorological Society*,  
 490 *122*(531), 689–719. <https://doi.org/10.1002/qj.49712253107>  
 491
- 492 Etminan, M., Myhre, G., Highwood, E. J., & Shine, K. P. (2016). Radiative forcing of carbon  
 493 dioxide, methane, and nitrous oxide: A significant revision of the methane radiative forcing.  
 494 *Geophysical Research Letters*, *43*(24), 12,614–12,623. <https://doi.org/10.1002/2016GL071930>  
 495
- 496 Feldman, D. R., Collins, W. D., Gero, P. J., Torn, M. S., Mlawer, E. J., & Shippert, T. R. (2015).  
 497 Observational determination of surface radiative forcing by CO<sub>2</sub> from 2000 to 2010. *Nature*,  
 498 *519*(7543), 339–343. <https://doi.org/10.1038/nature14240>  
 499
- 500 Feldman, D. R., Collins, W. D., Biraud, S. C., Risser, M. D., Turner, D. D., Gero, P. J., et al.  
 501 (2018). Observationally derived rise in methane surface forcing mediated by water vapour  
 502 trends. *Nature Geoscience*, *11*(4), 238–243. <https://doi.org/10.1038/s41561-018-0085-9>  
 503
- 504 Friedlingstein, P., Jones, M. W., O’Sullivan, M., Andrew, R. M., Hauck, J., Peters, G. P., et al.  
 505 (2019). Global Carbon Budget 2019. *Earth System Science Data*, *11*(4), 1783–1838.  
 506 <https://doi.org/10.5194/essd-11-1783-2019>  
 507
- 508 Gelaro, R., McCarty, W., Suárez, M. J., Todling, R., Molod, A., Takacs, L., et al. (2017). The  
 509 Modern-Era Retrospective Analysis for Research and Applications, Version 2 (MERRA-2).  
 510 *Journal of Climate*, *30*(14), 5419–5454. <https://doi.org/10.1175/JCLI-D-16-0758.1>  
 511
- 512 Harries, J. E., Brindley, H. E., Sagoo, P. J., & Bantges, R. J. (2001). Increases in greenhouse  
 513 forcing inferred from the outgoing longwave radiation spectra of the Earth in 1970 and 1997.  
 514 *Nature*, *410*(6826), 355–357. <https://doi.org/10.1038/35066553>  
 515
- 516 Hearty, T. J., Savtchenko, A., Tian, B., Fetzer, E., Yung, Y. L., Theobald, M., et al. (2014).  
 517 Estimating sampling biases and measurement uncertainties of AIRS/AMSU-A temperature and  
 518 water vapor observations using MERRA reanalysis. *Journal of Geophysical Research:*  
 519 *Atmospheres*, *119*(6), 2725–2741. <https://doi.org/10.1002/2013JD021205>  
 520
- 521 Hodnebrog, Ø., Etminan, M., Fuglestad, J. S., Marston, G., Myhre, G., Nielsen, C. J., et al.  
 522 (2013). Global warming potentials and radiative efficiencies of halocarbons and related

523 compounds: A comprehensive review. *Reviews of Geophysics*, 51(2), 300–378.  
 524 <https://doi.org/10.1002/rog.20013>  
 525  
 526 Hofmann, D. J., Butler, J. H., Dlugokencky, E. J., Elkins, J. W., Masarie, K., Montzka, S. A., &  
 527 Tans, P. (2006). The role of carbon dioxide in climate forcing from 1979 to 2004: introduction of  
 528 the Annual Greenhouse Gas Index. *Tellus B: Chemical and Physical Meteorology*, 58(5), 614–  
 529 619. <https://doi.org/10.1111/j.1600-0889.2006.00201.x>  
 530  
 531 Jiang, Y., Aumann, H.H., Wingyee-Lau, M., & Yung, Y.L. (2011). Climate change sensitivity  
 532 evaluation from AIRS and IRIS measurements. *Proc. SPIE* 8153, XVI (2011), doi:  
 533 <http://dx.doi.org/10.1117/12.892817>  
 534  
 535 Kato, S., Rose, F. G., Rutan, D. A., Thorsen, T. J., Loeb, N. G., Doelling, D. R., et al. (2018).  
 536 Surface Irradiances of Edition 4.0 Clouds and the Earth’s Radiant Energy System (CERES)  
 537 Energy Balanced and Filled (EBAF) Data Product. *Journal of Climate*, 31(11), 4501–4527.  
 538 <https://doi.org/10.1175/JCLI-D-17-0523.1>  
 539  
 540 Kok, J. F., Ridley, D. A., Zhou, Q., Miller, R. L., Zhao, C., Heald, C. L., et al. (2017). Smaller  
 541 desert dust cooling effect estimated from analysis of dust size and abundance. *Nature*  
 542 *Geoscience*, 10(4), 274–278. <https://doi.org/10.1038/ngeo2912>  
 543  
 544 Kramer, R. J., Matus, A. V., Soden, B. J., & L’Ecuyer, T. S. (2019). Observation-Based  
 545 Radiative Kernels From CloudSat/CALIPSO. *Journal of Geophysical Research: Atmospheres*,  
 546 2018JD029021. <https://doi.org/10.1029/2018JD029021>  
 547  
 548 Kühn, T., Partanen, A.-I., Laakso, A., Lu, Z., Bergman, T., Mikkonen, S., et al. (2014). Climate  
 549 impacts of changing aerosol emissions since 1996. *Geophysical Research Letters*, 41(13), 4711–  
 550 4718. <https://doi.org/10.1002/2014GL060349>  
 551  
 552 Leroy, S.S., Anderson, J.G., & Ohring, G. (2008) Climate Signal Detection Times and  
 553 Constraints on Climate Benchmark Accuracy Requirements. *Journal of Climate*. 21, 841–846  
 554  
 555 Loeb, N. G., Doelling, D. R., Wang, H., Su, W., Nguyen, C., Corbett, J. G., et al. (2018a).  
 556 Clouds and the Earth’s Radiant Energy System (CERES) Energy Balanced and Filled (EBAF)  
 557 Top-of-Atmosphere (TOA) Edition-4.0 Data Product. *Journal of Climate*, 31(2), 895–918.  
 558 <https://doi.org/10.1175/JCLI-D-17-0208.1>  
 559  
 560 Loeb, N., Thorsen, T., Norris, J., Wang, H., & Su, W. (2018b) Changes in Earth’s Energy  
 561 Budget during and after the “Pause” in Global Warming: An Observational  
 562 Perspective, *Climate* 6, 62.  
 563  
 564 Loeb, N. G., Rose, F. G., Kato, S., Rutan, D. A., Su, W., Wang, H., et al. (2019). Toward a  
 565 Consistent Definition between Satellite and Model Clear-Sky Radiative Fluxes. *Journal of*  
 566 *Climate*, 33(1), 61–75. <https://doi.org/10.1175/JCLI-D-19-0381.1>  
 567

- 568 Manners J, Edwards JM, Hill P, Thelen J-C. (2015). SOCRATES (Suite Of Community  
569 Radiative Transfer codes based on Edwards and Slingo) Technical Guide. Met Office, UK.  
570
- 571 Miller, R. L., Knippertz, P., Pérez García-Pando, C., Perlwitz, J. P., & Tegen, I. (2014). Impact  
572 of Dust Radiative Forcing upon Climate. In P. Knippertz & J.-B. W. Stuut (Eds.), *Mineral Dust:  
573 A Key Player in the Earth System* (pp. 327–357). Dordrecht: Springer Netherlands.  
574 [https://doi.org/10.1007/978-94-017-8978-3\\_13](https://doi.org/10.1007/978-94-017-8978-3_13)  
575
- 576 Mlynczak, M. G., Daniels, T. S., Kratz, D. P., Feldman, D. R., Collins, W. D., Mlawer, E. J., et  
577 al. (2016). The spectroscopic foundation of radiative forcing of climate by carbon dioxide.  
578 *Geophysical Research Letters*, 43(10), 5318–5325. <https://doi.org/10.1002/2016GL068837>  
579
- 580 Montzka, S. A., Dlugokencky, E. J., & Butler, J. H. (2011). Non-CO2 greenhouse gases and  
581 climate change. *Nature*, 476(7358), 43–50. <https://doi.org/10.1038/nature10322>  
582
- 583 Myhre, G., Shindell, D., Bréon, F.-M., Collins, W., Fuglestad, J., Huang, J., Koch, D.,  
584 Lamarque, J.-F., Lee, E., et al., (2013a). Anthropogenic and natural radiative forcing. In *Climate  
585 Change 2013: The Physical Science Basis. Contribution of Working Group I to the Fifth  
586 Assessment Report of the Intergovernmental Panel on Climate Change*. T.F. Stocker, D. Qin, G.-  
587 K. Plattner, M. Tignor, S.K. Allen, J. Doschung, A. Nauels, Y. Xia, V. Bex, and P.M. Midgley,  
588 Eds. Cambridge University Press, pp. 659-740, doi:10.1017/CBO9781107415324.018  
589
- 590 Myhre, G., Samset, B. H., Schulz, M., Balkanski, Y., Bauer, S., Bernsten, T. K., et al. (2013b).  
591 Radiative forcing of the direct aerosol effect from AeroCom Phase II simulations. *Atmospheric  
592 Chemistry and Physics*, 13(4), 1853–1877. <https://doi.org/10.5194/acp-13-1853-2013>  
593
- 594 Pendergrass, A. G., Conley, A., & Vitt, F. M. (2018). Surface and top-of-atmosphere radiative  
595 feedback kernels for CESM-CAM5. *Earth System Science Data*, 10(1), 317–324.  
596 <https://doi.org/10.5194/essd-10-317-2018>  
597
- 598 Philipona, R., Dürr, B., Marty, C., Ohmura, A., & Wild, M. (2004). Radiative forcing - measured  
599 at Earth's surface - corroborate the increasing greenhouse effect. *Geophysical Research Letters*,  
600 31(3). <https://doi.org/10.1029/2003GL018765>  
601
- 602 Pincus, R., Mlawer, E. J., Oreopoulos, L., Ackerman, A. S., Baek, S., Brath, M., et al. (2015).  
603 Radiative flux and forcing parameterization error in aerosol-free clear skies. *Geophysical  
604 Research Letters*, 42(13), 5485–5492. <https://doi.org/10.1002/2015GL064291>  
605
- 606 Pincus, R., Buehler, S. A., Brath, M., Jamil, O., Evans, F., Manners, J., et al. (2020). Benchmark  
607 calculations of radiative forcing by greenhouse gases. *Earth and Space Science Open Archive*,  
608 15. <https://doi.org/10.1002/essoar.10501550.1>  
609
- 610 Randles, C. A., Kinne, S., Myhre, G., Schulz, M., Stier, P., Fischer, J., et al. (2013).  
611 Intercomparison of shortwave radiative transfer schemes in global aerosol modeling: results from  
612 the AeroCom Radiative Transfer Experiment. *Atmospheric Chemistry and Physics*, 13(5), 2347–  
613 2379. <https://doi.org/10.5194/acp-13-2347-2013>



614  
 615 Raghuraman, S. P., Paynter, D., & Ramaswamy, V. (2019). Quantifying the Drivers of the Clear  
 616 Sky Greenhouse Effect, 2000–2016. *Journal of Geophysical Research: Atmospheres*, *124*(21),  
 617 11354–11371. <https://doi.org/10.1029/2019JD031017>  
 618  
 619 Ridley, D. A., Heald, C. L., Ridley, K. J., & Kroll, J. H. (2018). Causes and consequences of  
 620 decreasing atmospheric organic aerosol in the United States. *Proceedings of the National*  
 621 *Academy of Sciences*, *115*(2), 290. <https://doi.org/10.1073/pnas.1700387115>  
 622  
 623 Sayer, A. M., Munchak, L. A., Hsu, N. C., Levy, R. C., Bettenhausen, C., & Jeong, M.-J. (2014).  
 624 MODIS Collection 6 aerosol products: Comparison between Aqua’s e-Deep Blue, Dark Target,  
 625 and “merged” data sets, and usage recommendations. *Journal of Geophysical Research:*  
 626 *Atmospheres*, *119*(24), 13,965–13,989. <https://doi.org/10.1002/2014JD022453>  
 627  
 628 Shao, Y., Klose, M., & Wyrwoll, K.-H. (2013). Recent global dust trend and connections to  
 629 climate forcing. *Journal of Geophysical Research: Atmospheres*, *118*(19), 11,107–11,118.  
 630 <https://doi.org/10.1002/jgrd.50836>  
 631  
 632 Sherwood, S. C., Bony, S., Boucher, O., Bretherton, C., Forster, P. M., Gregory, J. M., &  
 633 Stevens, B. (2015). Adjustments in the Forcing-Feedback Framework for Understanding Climate  
 634 Change. *Bulletin of the American Meteorological Society*, *96*(2), 217–228.  
 635 <https://doi.org/10.1175/BAMS-D-13-00167.1>  
 636  
 637 Smith, C. J., Kramer, R. J., Myhre, G., Forster, P. M., Soden, B. J., Andrews, T., et al. (2018).  
 638 Understanding Rapid Adjustments to Diverse Forcing Agents. *Geophysical Research Letters*,  
 639 *45*(21), 12,023–12,031. <https://doi.org/10.1029/2018GL079826>  
 640  
 641 Smith, C. J., Kramer, R. J., Myhre, G., Alterskjær, K., Collins, W., Sima, A., et al. (2020).  
 642 Effective radiative forcing and adjustments in CMIP6 models. *Atmospheric Chemistry and*  
 643 *Physics*, *20*(16), 9591–9618. <https://doi.org/10.5194/acp-20-9591-2020>  
 644  
 645 Soden, B. J., Broccoli, A. J., & Hemler, R. S. (2004). On the Use of Cloud Forcing to Estimate  
 646 Cloud Feedback. *Journal of Climate*, *17*(19), 3661–3665. [https://doi.org/10.1175/1520-0442\(2004\)017<3661:OTUOCF>2.0.CO;2](https://doi.org/10.1175/1520-0442(2004)017<3661:OTUOCF>2.0.CO;2)  
 647  
 648  
 649 Soden, B. J., Held, I. M., Colman, R., Shell, K. M., Kiehl, J. T., & Shields, C. A. (2008).  
 650 Quantifying Climate Feedbacks Using Radiative Kernels. *Journal of Climate*, *21*(14), 3504–  
 651 3520. <https://doi.org/10.1175/2007JCLI2110.1>  
 652  
 653 Soden, B. J., Collins, W. D., & Feldman, D. R. (2018). Reducing uncertainties in climate models.  
 654 *Science*, *361*(6400), 326–327. <https://doi.org/10.1126/science.aau1864>  
 655  
 656 Stier, P., Schutgens, N. A. J., Bellouin, N., Bian, H., Boucher, O., Chin, M., et al. (2013). Host  
 657 model uncertainties in aerosol radiative forcing estimates: results from the AeroCom Prescribed  
 658 intercomparison study. *Atmospheric Chemistry and Physics*, *13*(6), 3245–3270.  
 659 <https://doi.org/10.5194/acp-13-3245-2013>

660  
 661 Susskind, J., Schmidt, G. A., Lee, J. N., & Iredell, L. (2019). Recent global warming as  
 662 confirmed by AIRS. *Environmental Research Letters*, *14*(4), 044030.  
 663 <https://doi.org/10.1088/1748-9326/aafd4e>  
 664  
 665 Taylor, K., Ronald, S., & Meehl, G. (2011). An overview of CMIP5 and the Experiment Design.  
 666 *Bulletin of the American Meteorological Society*, *93*, 485–498. [https://doi.org/10.1175/BAMS-](https://doi.org/10.1175/BAMS-D-11-00094.1)  
 667 [D-11-00094.1](https://doi.org/10.1175/BAMS-D-11-00094.1)  
 668  
 669 Tobin, D. C., Revercomb, H. E., Knuteson, R. O., Lesht, B. M., Strow, L. L., Hannon, S. E., et  
 670 al. (2006). Atmospheric Radiation Measurement site atmospheric state best estimates for  
 671 Atmospheric Infrared Sounder temperature and water vapor retrieval validation. *Journal of*  
 672 *Geophysical Research: Atmospheres*, *111*(D9). <https://doi.org/10.1029/2005JD006103>  
 673  
 674 Thorsen, T. J., Kato, S., Loeb, N. G., & Rose, F. G. (2018). Observation-Based Decomposition  
 675 of Radiative Perturbations and Radiative Kernels. *Journal of Climate*, *31*(24), 10039–10058.  
 676 <https://doi.org/10.1175/JCLI-D-18-0045.1>  
 677  
 678 Thorsen, T. J., Winker, D. M., & Ferrare, R. A. (2020). Uncertainty in observational estimates of  
 679 the aerosol direct radiative effect and forcing. *Journal of Climate*, 1–63.  
 680 <https://doi.org/10.1175/JCLI-D-19-1009.1>  
 681  
 682 Trenberth, K. E., Fasullo, J. T., & Balmaseda, M. A. (2014). Earth’s Energy Imbalance. *Journal*  
 683 *of Climate*, *27*(9), 3129–3144. <https://doi.org/10.1175/JCLI-D-13-00294.1>  
 684  
 685 Trenberth, K. E., Zhang, Y., & Fasullo, J. T. (2015). Relationships among top-of-atmosphere  
 686 radiation and atmospheric state variables in observations and CESM. *Journal of Geophysical*  
 687 *Research: Atmospheres*, *120*(19), 10,074–10,090. <https://doi.org/10.1002/2015JD023381>  
 688  
 689 Vial, J., Dufresne, J.-L., & Bony, S. (2013). On the interpretation of inter-model spread in  
 690 CMIP5 climate sensitivity estimates. *Climate Dynamics*, *41*(11), 3339–3362.  
 691 <https://doi.org/10.1007/s00382-013-1725-9>  
 692  
 693 Watson-Parris, D., Bellouin, N., Deaconu, L. T., Schutgens, N. A. J., Yoshioka, M., Regayre, L.  
 694 A., et al. (2020). Constraining Uncertainty in Aerosol Direct Forcing. *Geophysical Research*  
 695 *Letters*, *47*(9), e2020GL087141. <https://doi.org/10.1029/2020GL087141>  
 696  
 697 Zhang, B., Kramer, R. J., & Soden, B. J. (2019). Radiative Feedbacks Associated with the  
 698 Madden–Julian Oscillation. *Journal of Climate*, *32*(20), 7055–7065.  
 699 <https://doi.org/10.1175/JCLI-D-19-0144.1>  
 700  
 701 Zhang, Q., Zheng, Y., Tong, D., Shao, M., Wang, S., Zhang, Y., et al. (2019). Drivers of  
 702 improved PM2.5 air quality in China from 2013 to 2017. *Proceedings of the National Academy*  
 703 *of Sciences*, *116*(49), 24463–24469. <https://doi.org/10.1073/pnas.1907956116>  
 704  
 705

706  
 707 **Figure 1.** Global-mean a) net, b) longwave (LW) and c) shortwave (SW) total radiative flux  
 708 anomalies from 2003 through 2018 as measured by CERES (black) and the contribution to that  
 709 total from the sum of radiative responses (red). Respective trendlines are displayed as dashed  
 710 lines. Uncertainty of  $\pm 2\sigma$  is shown for each timeseries, computed as described in the Methods.  
 711 Linear trends and 95% confidence intervals are provided in text.

712  
 713 **Figure 2.** Global-mean a) total, b) longwave (LW) and c) shortwave (SW) instantaneous  
 714 radiative forcing (IRF) estimated from the radiative kernel technique for CERES/AIRS (red) and  
 715 MERRA-2 (blue). Additional calculations of greenhouse gas-only IRF are also shown using  
 716 empirical formulas (green) and the SOCRATES radiative transfer model (gray). For reference,  
 717 the trendline for total radiative flux anomalies (Fig 1a) is displayed with the total IRF as a black  
 718 dashed line. Uncertainty of  $\pm 2\sigma$  is shown with shading for each timeseries, computed as  
 719 described in the Methods. Linear trends and 95% confidence intervals are provided in text and  
 720 in Table 1.

721  
 722 **Figure 3.** Local linear trends from 2003 through 2018 in all-sky shortwave instantaneous  
 723 radiative forcing (SW IRF) diagnosed in a) CERES/AIRS observations and b) MERRA-2  
 724 reanalysis using the radiative kernel differencing technique and c) from direct output of  
 725 MERRA-2 aerosol IRF. Also, local linear trends over the same time period are shown for aerosol  
 726 optical depth (AOD) from d) MODIS and e) MERRA-2.

727

728 **Table 1.** Global-mean linear trends ( $\text{W}/\text{m}^2/\text{year}$ ) and 95% confidence bounds in instantaneous  
729 radiative forcing estimated using the radiative kernel differencing technique (first two rows) and  
730 MERRA-2 flux diagnostics (third row).

731